pISSN 2384-1095
eISSN 2384-1109

iMRI 2015;19:76-87

http://dx.doi.org/10.13104/imri.2015.19.2.76

iMRI
Investigative Magnetic Resonance Imaging

Effect of Manganese Content on the Magnetic Susceptibility of Ferrous-Manganese Alloys: Correlation between Microstructure on X-Ray Diffraction and Size of the Low-Intensity Area on MRI

Sung Won Youn[1], Moon Jung Kim[2], Seounghoon Yi[2], Hyun Jin Ahn[3], Kwan Kyu Park[3], Jongmin Lee[4], Young-Cheol Lee[5]

[1]Department of Radiology, Catholic University of Daegu, School of Medicine, Daegu, Korea
[2]Department of Materials Science and Metallurgical Engineering, Kyungpook National University, Daegu, Korea
[3]Department of Pathology, Catholic University of Daegu, School of Medicine, Daegu, Korea
[4]Department of Radiology, Kyungpook National University, School of Medicine, Daegu, Korea
[5]Korea Institute of Industrial Technology Dongnam Technology Application Division, Pusan, Korea

Original Article

Received: May 15, 2015
Revised: June 11, 2015
Accepted: June 15, 2015

Correspondence to:
Sung Won Youn, M.D.
Department of Radiology, Catholic University of Daegu, School of Medicine, 3056-6 Daemyung-4 Dong, Nam-gu, Daegu 705-718, Korea.
Tel. +82-53-650-4076
Fax. +82-53-650-4339
Email: ysw10adest@cu.ac.kr

Purpose: There is an ongoing search for a stent material that produces a reduced susceptibility artifact. This study evaluated the effect of manganese (Mn) content on the MRI susceptibility artifact of ferrous-manganese (Fe-Mn) alloys, and investigated the correlation between MRI findings and measurements of Fe-Mn microstructure on X-ray diffraction (XRD).

Materials and Methods: Fe-Mn binary alloys were prepared with Mn contents varying from 10% to 35% by weight (i.e., 10%, 15%, 20%, 25%, 30%, and 35%; designated as Fe-10Mn, Fe-15Mn, Fe-20Mn, Fe-25Mn, Fe-30Mn, and Fe-35Mn, respectively), and their microstructure was evaluated using XRD. Three-dimensional spoiled gradient echo sequences of cylindrical specimens were obtained in parallel and perpendicular to the static magnetic field (B0). In addition, T1-weighted spin echo, T2-weighted fast spin echo, and T2*-weighted gradient echo images were obtained. The size of the low-intensity area on MRI was measured for each of the Fe-Mn binary alloys prepared.

Results: Three phases of α'-martensite, γ-austenite, and ε-martensite were seen on XRD, and their composition changed from α'-martensite to γ-austenite and/or ε-martensite, with increasing Mn content. The Fe-10Mn and Fe-15Mn specimens comprised α'-martensite, the Fe-20Mn and Fe-25Mn specimens comprised γ+ε phases, and the Fe-30Mn and Fe-35Mn specimens exhibited a single γ phase. The size of the low-intensity areas of Fe-Mn on MRI decreased relative to its microstructure on XRD with increasing Mn content.

Conclusion: Based on these findings, proper conditioning of the Mn content in Fe-Mn alloys will improve its visibility on MR angiography, and a Mn content of more than 25% is recommended to reduce the magnetic susceptibility artifacts on MRI. A reduced artifact of Fe-Mn alloys on MRI is closely related to the paramagnetic

constitution of γ-austenite and/or ε-martensite.

Keywords: Stent; Ferro-manganese alloy; Manganese; Magnetic resonance angiography; Artifact; X-ray diffraction

INTRODUCTION

The effectiveness of the metallic stent for reconstructing stenotic or occluded vascular lesions has been established (1, 2). However, the presence of a metallic stent itself introduces its own potential risks, with the possibility of inducing a serious biologic reaction, including thrombosis or restenosis (3). Given that the stent itself is potentially capable of inducing a biologic reaction, the concept of a bioabsorbable stent, which would disappear after functioning for only the short period of time that it is needed, has emerged as an attractive alternative option (4-7). This has prompted continued efforts to find materials that could be used to produce a bioabsorbable stent. Ferrous (Fe) alloys typically exhibit great strength combined with reasonable ductility, which is important for the reliability of a stent material (8-12). However, common Fe alloys, such as stainless steel, are designed to resist biodegradation. In order to be biodegradable, the corrosion rate needs to be increased, but even pure Fe exhibits a low corrosion rate. The search for a combinatory element to enhance biodegradability led to the use of manganese (Mn) as an alloying element; the Fe-Mn combination was found to exhibit a faster corrosion rate than pure Fe (10-12). However, as with stainless steel, a major limitation of the clinical application of ferrous-based alloys is their high magnetic susceptibility. Since magnetic resonance angiography (MRA) is widely used to evaluate vascular patency after stent placement, stents with a low magnetic susceptibility would be the ideal choice (13-16). The magnetic susceptibility of such alloys was thought to be closely associated with its microstructure, and previous authors have reported on the phase constitution and microstructure of Fe-Mn alloys (10, 11). However, the correlation between the magnetic susceptibility of these alloys on MRA and their microstructure has not been reported.

The aim of this study was to determine the effect of varying the Mn content on the susceptibility artifact of Fe-Mn alloys on MRI, and to explain the findings in the context of its microstructure, as revealed by X-ray diffraction (XRD).

MATERIAL AND METHODS

Preparation of the Specimens and Microstructural Analysis

Binary Fe-Mn alloy ingots with nominal compositions (i.e., 10%, 15%, 20%, 25%, 30%, and 35% Mn by weight; designated as Fe-10Mn, Fe-15Mn, Fe-20Mn, Fe-25Mn, Fe-30Mn, and Fe-35Mn, respectively) were prepared using an arc-melting technique in an argon atmosphere using electrolytic Fe (> 99.99%) and Mn (> 99.7%) chips. The compositional homogeneity was secured by

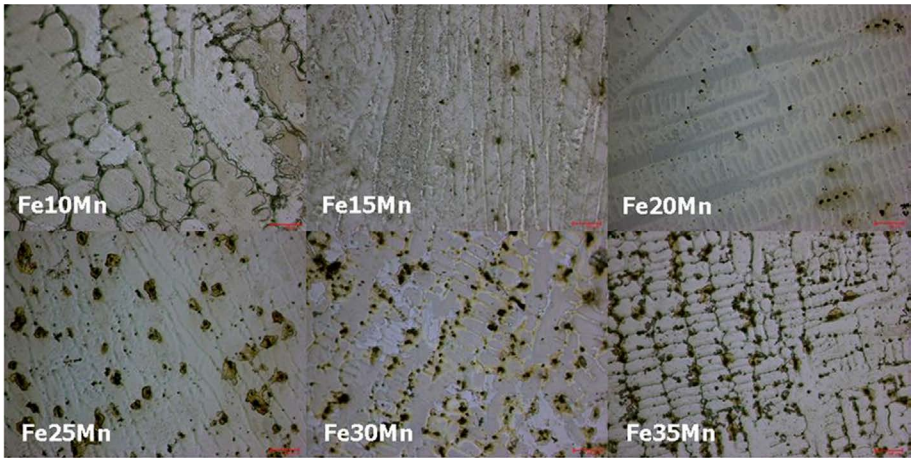

Fig. 1. Optical micrographs (× 100) of arc-melted ingots with the nominal compositions (i.e., 10%, 15%, 20%, 25%, 30%, and 35% Mn by weight; designated as Fe-10Mn, Fe-15Mn, Fe-20Mn, Fe-25Mn, Fe-30Mn, and Fe-35Mn, respectively). A typical dendritic structure was observed with zones of Mn aggregation between dendritic arms. Bar = 100 μm.

remelting each ingot at least three times. Some of the Mn evaporated during the arc-melting process due to the high vapor pressure of this element, thus reducing the actual percentage of Mn in each of the nominated samples (Table 1). The rod samples were prepared by casting the ingot into a copper mold with a cylindrical shape having dimensions of 4 mm × 15 mm, or 2.5 mm × 20 mm (diameter × length) using a suction-casting method, and then subjecting them to annealing for tissue homogenization.

The microstructure of arc-melted ingots and suction-cast rods were observed using optical microscopy (Fig. 1). The constituent phases were analyzed by XRD with Cu radiation (CuK_{α}, λ = 0.1541 nm). The chemical compositions of the arc-melted ingots were measured by an X-ray fluorescence analyzer using pure-metal references. Microhardness data were obtained with a Vickers microhardness tester by applying a load of 500 g for 10 seconds. For each data point, ten indentations were made to obtain a reliable microhardness value.

Acquisition of MRI Scans and Artifact Measurement

Settling of the specimen

The cylindrical rod was imaged while immersed in copper sulfate ($CuSO_4$) solution at room temperature, according to the guidelines of the ASTM F2119-01 standard of the American Society of Testing and Materials (17) (Fig. 2). The rod was fixed in position using a polyester string, within an acryl-polypropylene container filled with $CuSO_4$ at a concentration of 1 g/l, to minimize motion under the magnetic field and the susceptibility effect by the surrounding materials. The acryl container was constructed so that the specimen could be positioned 4 cm from all adjacent surfaces. Two 1 mm-sized holes were drilled at each end of the cylindrical specimen, 1 cm away from the ends, to allow it to be fixed in the container using polyester string.

Acquisition of MR images

MRI was conducted with a 1.5-T unit (Signa Excite, GE Healthcare, Milwaukee, WI, USA) and an eight-channel head coil. The imaging sequence included three-dimensional (3D) spoiled gradient echo (SPGR) imaging for the 4 mm × 15 mm specimens, and T1-weighted imaging (T1WI), T2-weighted imaging (T2WI), 3D SPGR imaging, and T2*-weighted gradient echo imaging (T2*-GRE) for the 2.5 mm × 20 mm specimens.

To determine the effect of location relative to the static magnetic field (B0), the longitudinal axis of the 4 mm × 15 mm rod was placed either parallel or perpendicular to B0 (18,

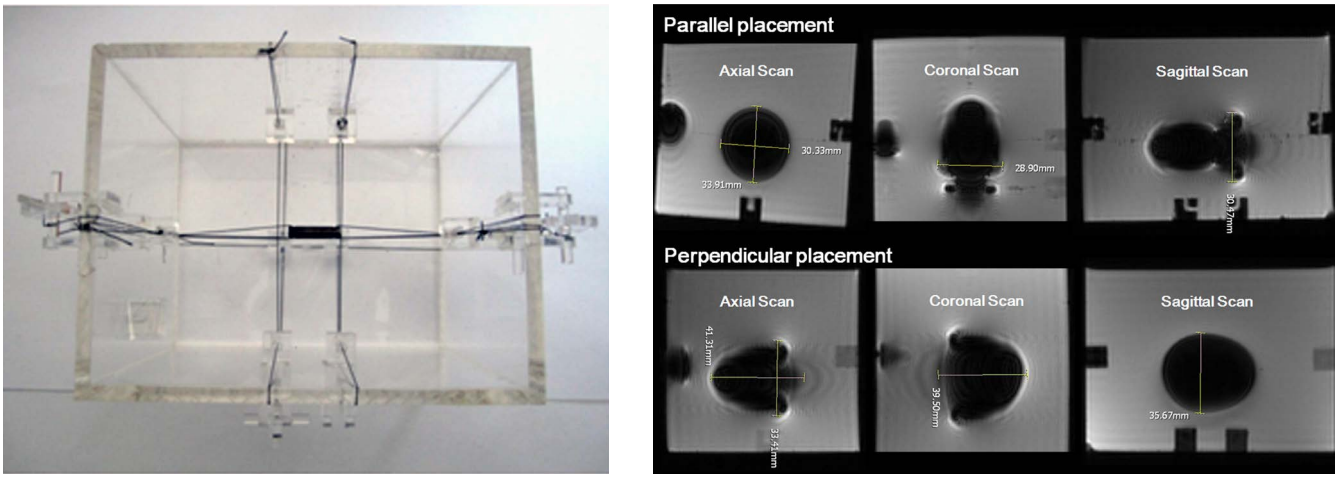

a b

Fig. 2. Acquisition of MR images for various specimen locations and scanning planes, and measurement of the susceptibility artifact. (a) Photograph of the device designed for fixing the specimen to yield an MR image without disturbing the adjacent material in any plane. The cylindrical alloy rod was fixed in position with a polyester string within a container filled with $CuSO_4$ solution. (b) The cylindrical rod (Fe25Mn; 4 mm × 15 mm) was placed parallel (upper row) or perpendicular (lower row) to B0. Three-dimensional spoiled gradient echo sequences (3D SPGR) were obtained in the axial, coronal, and sagittal planes, in that order. The maximum diameter of the resulting hypointensity was measured on a picture archiving system to assess the size of the susceptibility artifact.

19). The axial, coronal, and sagittal planes of 3D SPGR were recorded for each placement. Six images (two locations relative to B0 × 3 planes per each placement) were obtained for each $Fe_{100-x}Mn_x$ alloy. The following parameters were used: repetition time (TR) = 8.6 ms, echo time (TE) = 2.2 ms, flip angle = 15°, bandwidth = 15.63 kHz, acquisition matrix = 256 × 256 pixels, field of view = 200 mm × 200 mm, and slice thickness = 3 mm, with 1.5-mm intervals.

Additional MRI sequences were obtained for the 2.5 mm × 20 mm rods placed parallel to B0 to allow a comparison of the pattern of susceptibility artifacts between the fast spin echo (FSE) and gradient echo (GRE) sequences. The effect of homogenization heat treatment at 1200°C followed by air cooling on the susceptibility artifact, was evaluated by comparing the size of the low-intensity area on MRI, with and without heat treatment. The following image acquisition parameters were used - for T1WI: TR = 450 ms, TE = 14 ms, and flip angle = 90°; for T2WI: TR = 4400 ms, TE = 95.7 ms, flip angle = 90°, and echo train length = 16; and for T2*-GRE: TR = 567 ms, TE = 15 ms, and flip angle = 20°. The following parameters applied to all the three aforementioned sequences: acquisition matrix = 320 × 224 pixels, field of view = 180 mm × 180 mm, and slice thickness = 5 mm, with 7-mm intervals.

Measurement of low-intensity area on MRI

The maximum distance from the device boundary to the edge of the artifact is typically measured in one cross-section of the specimen with the maximum diameter perpendicular to the long axis. A digital ruler in a picture archiving system was used to measure the required distances (in millimeters). The low-intensity length ratio was defined as "maximum length of the low-intensity area in mm/actual length (i.e. 20 mm)", and the low-intensity diameter ratio was defined as "maximum diameter of low-intensity area in mm/actual diameter (i.e. 2.5 mm)".

MTT Cytotoxicity Test

The effects of Fe-Mn alloys on cell viability were assessed by an indirect contact method based on the MTT [3-(4,5-dimethylthiazol-2-yl)-2,5-diphenyltetrazoliumbromide, Sigma, MO, USA] assay (20, 21). Disk-shaped (2 mm thick and 10 mm in diameter) Fe-Mn alloy samples (Fe-20Mn, Fe-25Mn, and Fe-35Mn) were used to provide a large surface area. The disks were first sterilized with 75% ethanol and rinsed with phosphate-buffered saline. Alloy extracts were prepared using serum-free Dulbecco's modified Eagle's medium (DMEM, Gibco-BRL, Gaithersburg, MD, USA), with an extraction-medium:surface area ratio of 1.25 ml/cm^2, in a humidified atmosphere with 5% CO_2 at 37°C for 72 h. The supernatant was collected and centrifuged to prepare the extraction medium, then refrigerated at 4°C before being used in the cytotoxicity test.

Murine L-929 fibroblast cells (American Type Culture Collection, Rockville, MD, USA) were cultured in DMEM with 10% fetal bovine serum (FBS, Gibco), 100 U/ml penicillin, and 100 mg/ml streptomycin (Gibco BRL) at 37°C in a humidified atmosphere with 5% CO_2. Cells were

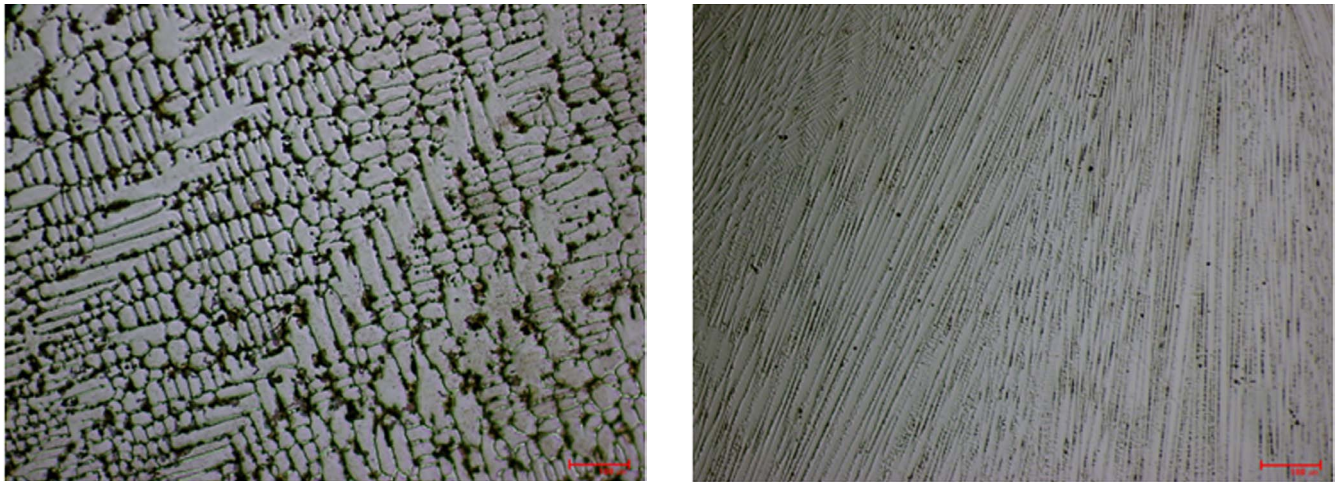

a b

Fig. 3. Optical micrographs (× 100) of specimens with the nominal compositions $Fe_{65}Mn_{35}$ specimens (wt %). (a) Arc-melted ingots, (b) suction-cast specimens. Very fine dendrite structures were formed, with dendrites having a relatively high Mn content being formed due to a relatively high solidification rate during suction casting. Bar = 100 μm.

seeded in 96-well cell culture plates at a density of 5×10^3 cells/100 µl of medium in each well, and incubated for 24 h to allow attachment. The medium was then replaced with 100 µl of the previously prepared extracts (treated cells) or fresh medium (control cells). After incubating the cells in a humidified atmosphere with 5% CO_2 at 37°C for 1, 2, or 4 days, the 96-well cell culture plates were observed using an optical microscope, after which 10 µl of MTT solution was added to each well. The plates were incubated for 4 h at 37°C, and finally the MTT-containing medium was removed by aspiration, and 100 µl of dimethylsulfoxide solution was added to each well. The absorbance was measured at 570 nm using a microplate reader (BMG LABTECH, Ortenberg, Germany).

Since the number of living cells is directly related to the cell metabolism from MTT to formazan detected at an absorbance of 570 nm, the viability was measured as follows:

viability (%) = (100×OD570e)/OD570b,

where OD570e is the mean absorbance of the extract of the test sample, and OD570b is the mean absorbance of the blank solution.

Cell cytotoxicity was assessed for Fe-Mn alloy extract concentrations of 50% and 100%. The cell survival in the 50% extract solution was higher than in the 100% extract solution, which suggests that the data were reliable.

RESULTS

Microstructure of Arc-Melted Ingots and Suction-Cast Rods

Optical micrographs of arc-melted ingots revealed a typical dendritic structure, with Mn segregation zones between the dendrite arms (Fig. 3). The spaces between the primary dendrite arms tend to decrease with increasing Mn content in the alloy, while the degree of Mn segregation increased, as evidenced by the dark areas or overetched regions between the dendrite arms. Thus, the fractions of overetched regions in the optical micrographs increased with the Mn content. For the suction-cast rods, very fine dendrite structures were observed due to the relatively high solidification rate during suction casting. Therefore, the degree of Mn segregation between the dendrite arms was significantly decreased. That is, dendrites with a relatively high Mn content were formed due to the high degree of undercooling attributed to the high solidification rate. Detailed experimental results regarding the effects of the solidification rate on phase transformations of the Fe-Mn alloys will be reported in a separate article.

Figure 4 shows the microhardness of the alloy specimens with different Mn contents. For those samples with a Mn content of < 30%, the hardness values were higher than 200 HV.

XRD of Arc-Melted Ingots and Suction-Cast Rods

The XRD spectra of arc-melted ingots exhibited

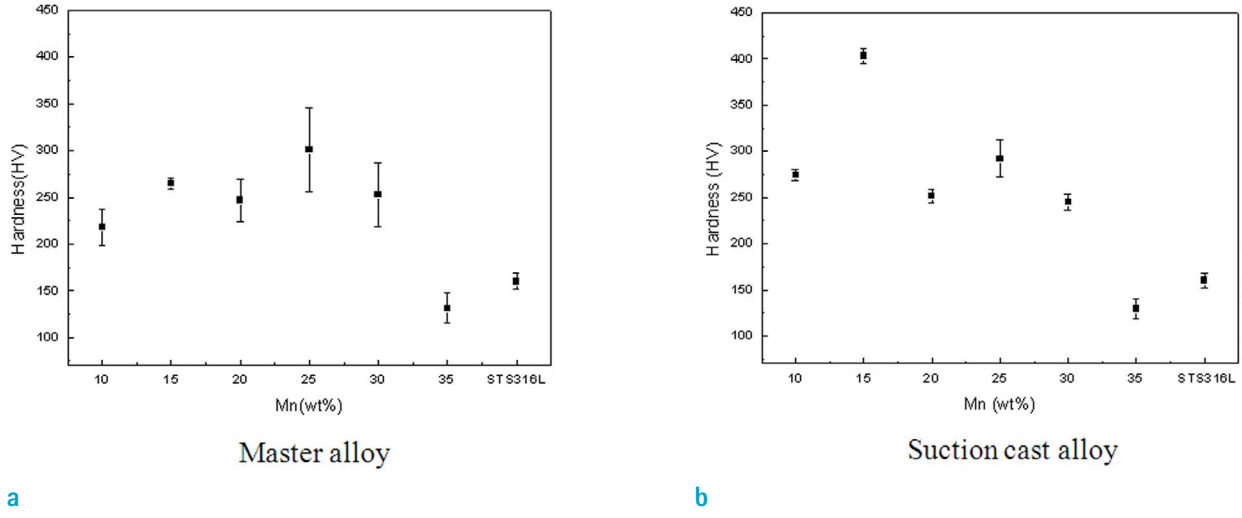

Fig. 4. Microhardness of the (a) arc-melted and (b) suction-cast specimens with the nominal compositions $Fe_{100-x}Mn_x$ (wt %). The hardness values were > 200 HV for the samples with an Mn content of < 30%.

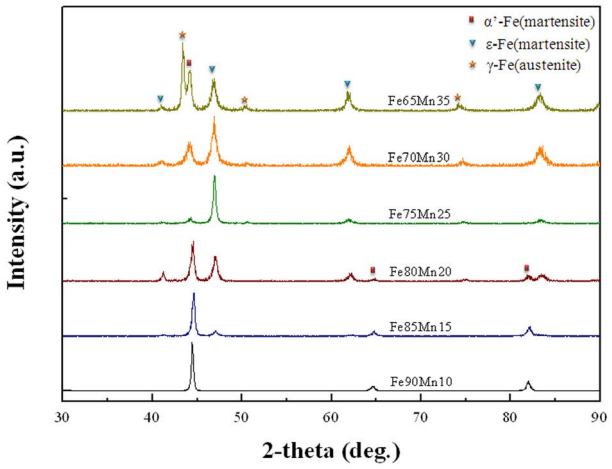

a

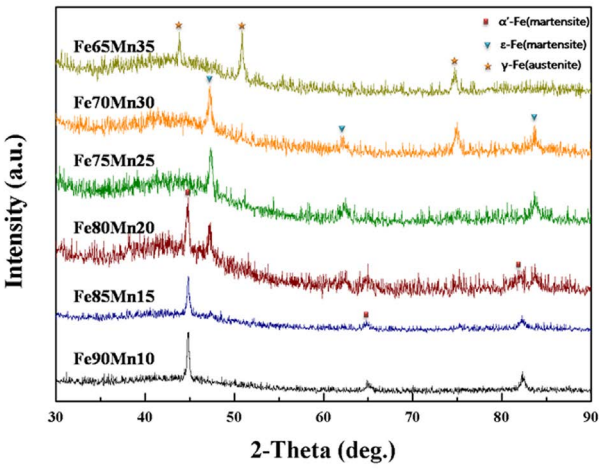

b

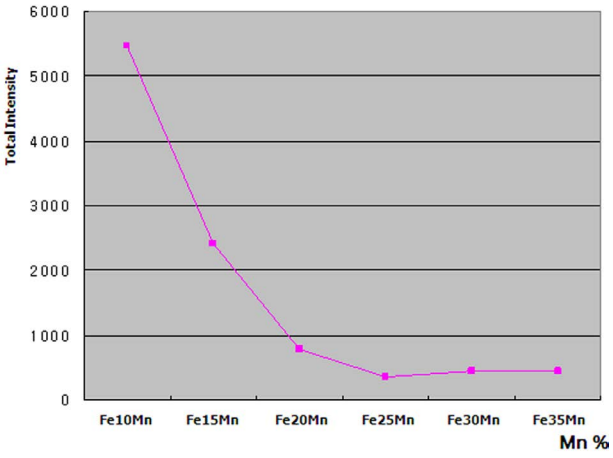

c

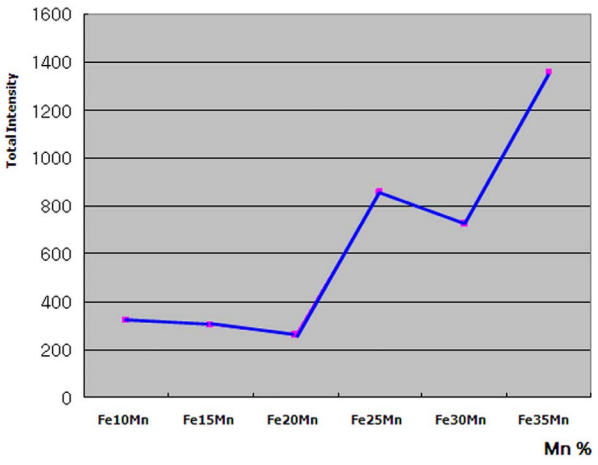

d

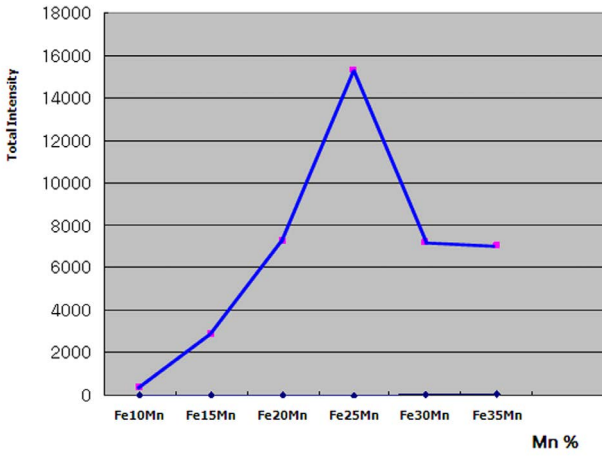

e

Fig. 5. The XRD spectra of (a) arc-melted ingots and (b) suction-cast specimens with the nominal compositions $Fe_{100-x}Mn_x$ (wt %) showing the phase identification and distribution. Diffraction peaks corresponding to α'-martensite (rectangle), γ-austenite (asterisk), and ε-martensite (triangle) are indicated. The amplitudes of the peaks found at positions corresponding to the 2-θ interval of (c) α'-martensite (63.0-66.0°), (d) γ-austenite (49.0-52.0°), and (e) ε-martensite (46.0-48.0°) can be observed to differ with the alloy Mn content.

diffraction peaks corresponding to α'-martensite, γ-austenite, and ε-martensite (Fig. 5a). For the suction-cast rods, as mentioned above, very fine dendrite structures with relatively high Mn contents were formed due to the high solidification rate, and the formation of α'-martensite tended to be suppressed, as inferred by the XRD results (Fig. 5b). The relative peak intensity data corresponding to each phase (Fig. 5c-e) suggests that γ-austenite is effectively stabilized by the addition of Mn; that is, the proportion of γ-austenite increases markedly with the Mn content. Some of the γ-austenite was transformed into ε-martensite rather than α'-martensite during the postsolidification phase transformations of ingots with a Mn content of > 20%. In other words, when the Mn content is low, γ-austenite tends to be transformed into α'-martensite rather than ε-martensite. The phases detected by the XRD analysis are summarized in Table 1.

Size of the Low-Intensity Area on MRI

The 4 mm × 15 mm cylindrical specimen

The rod-shaped specimen appeared as a bullet-like

Table 1. Composition of Mn in Arc-Melted Fe-Mn Ingots Obtained by X-Ray Fluorescence, and the Constituent Phases in Each Specimen

$Fe_{100-x}Mn_x$	Mn (wt %)	Phases in arc-melted ingots	Phases in suction-cast rods
$Fe_{90}Mn_{10}$	7.9	α'-martensite	α'-martensite
$Fe_{85}Mn_{15}$	12.5	α'-martensite + (ε-martensite)	α'-martensite
$Fe_{80}Mn_{20}$	15.6	α'-martensite + ε-martensite	α'-martensite + ε-martensite
$Fe_{75}Mn_{25}$	20.6	(α'-martensite) + ε-martensite	ε-martensite + (γ-austenite)
$Fe_{70}Mn_{30}$	25.0	α'-martensite + ε-martensite + γ-martensite	ε-martensite + γ-austenite
$Fe_{65}Mn_{35}$	30.1	γ-austenite + ε-martensite + α-martensite	γ-austenite

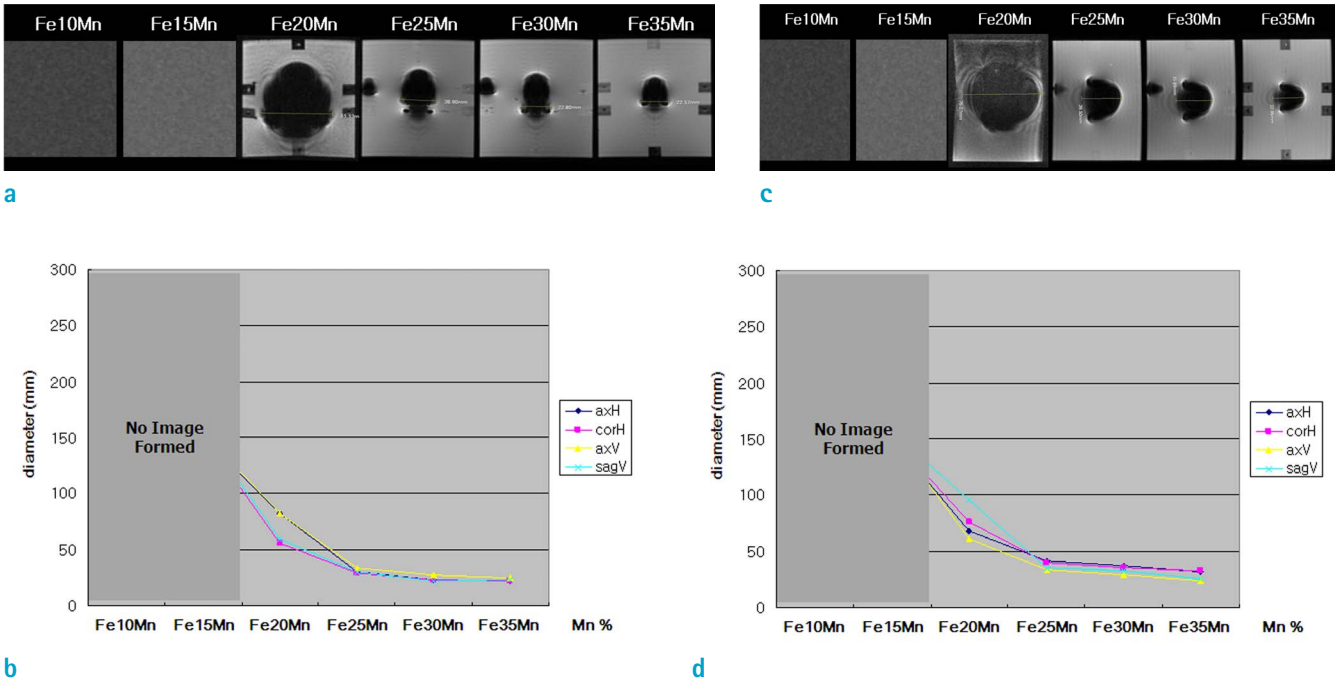

Fig. 6. The low-intensity area of the Fe-Mn alloys on 3D SPGR according to Mn content. The cylindrical specimen (4 × 15 mm) was placed either parallel (a, b) or perpendicular (c, d) to B0. The size of the low-intensity area decreased rapidly between, as the Mn content increased from 20% to 25%, and reached a plateau at 30-35% in both conditions. The horizontal (axH) and vertical (axV) maximum diameters were measured in the axial scanning planes. The horizontal (corH) and vertical (sagV) maximum diameters were measured in the coronal and sagittal planes.

low-intensity area parallel to B0, in images taken both perpendicular and parallel to B0. No image could be discerned with either Fe-10Mn or Fe-15Mn on 3D SPGR, but the presence of a specimen was confirmed within the $CuSO_4$ container by T1WI. For further increases in Mn content (i.e., Fe-20Mn, Fe-25Mn, Fe-30Mn, and Fe-35Mn), the largest diameter of the low-intensity area in the three scanning planes serially decreased, falling into the ground at Fe-25Mn, in both the perpendicular and parallel positions (Fig. 6).

The 2.5 mm × 20 mm cylindrical specimen

As Mn content increased, the size of the low-intensity area decreased, markedly between 20% and 25% (i.e., Fe-20Mn and Fe-25Mn), reaching a plateau at 25-30% (Fig. 7). These findings were commonly observed for the longitudinal length and transverse diameter of the cylindrical specimen with a parallel location to B0.

These MRI findings, related to the Mn content of Fe-Mn alloy, were similar in 3D SPGR, T2*-GRE, T1WI, and T2WI sequences. By comparison, among these various MRI sequences, both the length ratio and the diameter

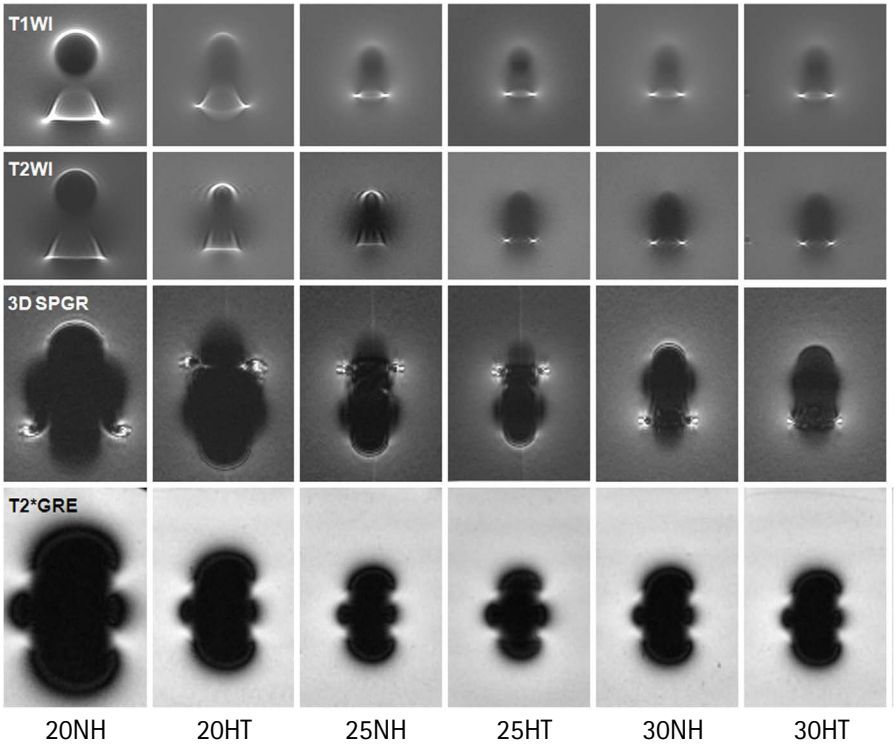

a

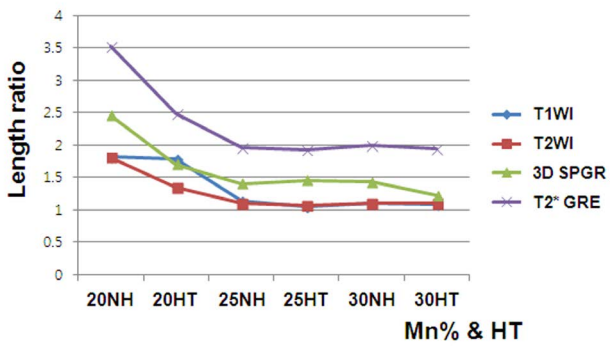

b

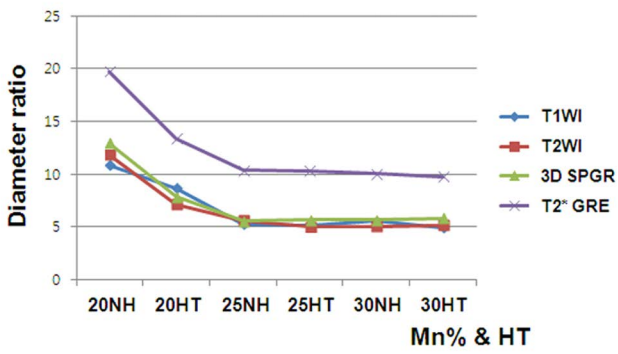

c

Fig. 7. Susceptibility artifacts on various MRI sequences for different alloy Mn contents, and with or without homogenization heat treatment (HT). (a) T1WI (first row), T2WI (second row), 3D SPGR (third row), and T2*-GRE (fourth row) of a 2.5 mm × 20 mm cylindrical rod parallel to B0. (b) Length ratio (length of maximum low-intensity area in mm/actual length of 20 mm) and (c) diameter ratio (diameter of maximum low-intensity area in mm/actual diameter of 2.5 mm) showing that the susceptibility artifact decreased rapidly for 20-25% Mn, and reached a plateau for 30% Mn. The HT decreased the size of the low-intensity area for 20% Mn but not for 25-30% Mn. 20NH (Mn 20% without HT); 20HT (Mn 20% with HT); 25NH (Mn 25% without HT); 25HT (Mn 25% with HT); 30NH (Mn 30% without HT); 30HT (Mn 30% with HT).

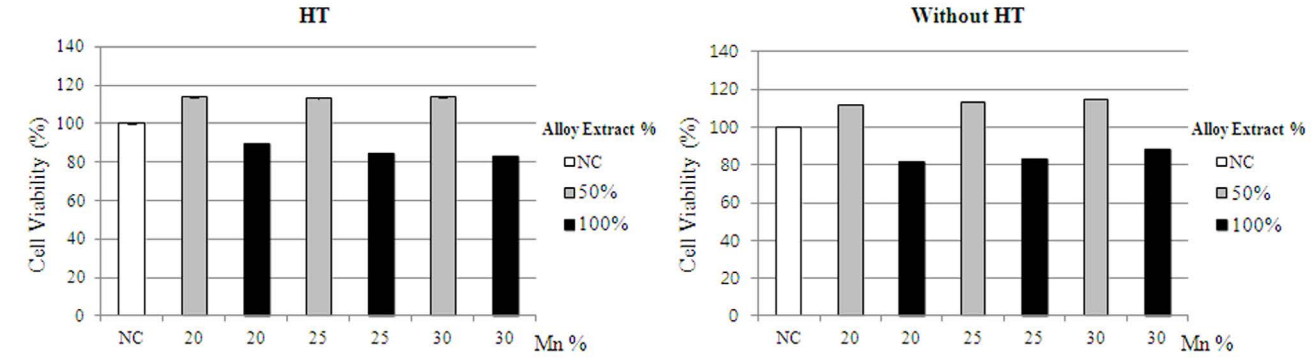

a

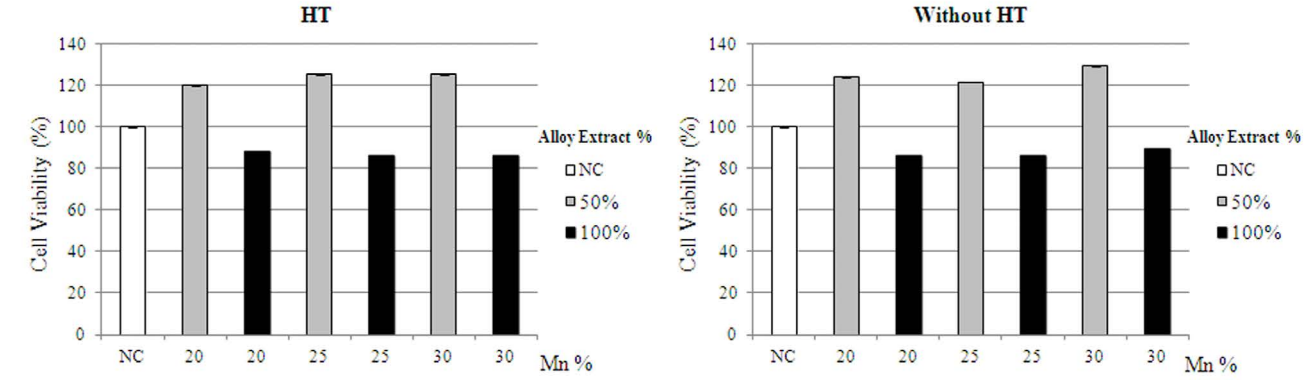

b

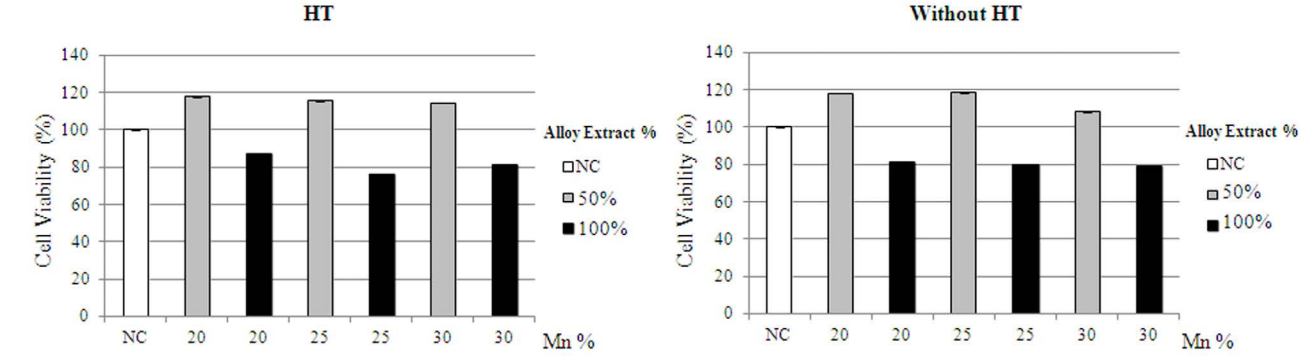

c

Fig. 8. MTT assays according to Mn content and HT at alloy extract concentrations of 50% and 100%. The cell viability for each Mn content (i.e., 20%, 25%, and 30%) was estimated to be 80-90% at day 1 (a) and day 2 (b), and 70-80% on day 4 (c). NC = normal control

ratio were lowest with FSEs including T1WI and T2WI, and highest with T2*-GRE (1.83 times the average FSE). The size of the low-intensity ratios on 3D SPGR fell between those of FSEs and T2*-GRE. As for the effect of specimen geometry, the diameter ratio was larger than the length ratio in all sequences (4.96 times the average). In addition, homogenizing heat treatment decreased the susceptibility artifact for Fe-20Mn, but not for either Fe-25Mn or Fe-30Mn.

Evaluation of Cell Viability

The cell viabilities in extracts of Fe-20Mn, Fe-25Mn, and Fe-30Mn were estimated to be > 80-90% at days 1 and 2, and > 70-80% on day 4 (Fig. 8). Since the cell survival rate was > 70% of that in the blank solution, it can be concluded that all the extracts (i.e., Fe-20Mn, Fe-25Mn, and Fe-30Mn) were noncytotoxic. The cell survival did not differ between the groups with or without homogenizing heat treatment, or with the Mn content.

DISCUSSION

Catheter angiography, which is the gold-standard method of imaging vascular lesions, is an invasive procedure that requires catheterization, iodine contrast injection, and radiation exposure. MRA without catheterization is a noninvasive procedure, and useful for follow-up imaging of stent placement; it shows cross-sectional views of the stented arteries (22-24). However, metallic stents may cause signal dropout on MRI due to their inherent magnetic susceptibility (14, 24). Conventional Fe-based metallic stents produce severe ferromagnetic artifacts, which obscure the imaging in the vicinity of the stent, rendering pure-Fe-based stents unsuitable for MRA. To overcome this pitfall, Fe-Mn alloys were presumed to be promising stent materials with excellent mechanical strength and biodegradability (10-12). Therefore, the present study sought to determine the optimal alloy conditions for minimizing susceptibility artifacts.

The XRD spectra of Fe-Mn alloys obtained in this study comprised three phases: ferromagnetic α′-martensite, paramagnetic γ-austenite, and ε-martensite. The portion of α′-martensite decreased markedly and that of γ -austenite increased markedly with increasing alloy Mn content. At a Mn content of < 20%, γ-austenite tended to transform into α′-martensite rather than ε-martensite, and the specimen mainly carried the phase of α′-martensite, while ε-martensite peaked with Fe-25Mn. Some of the γ-austenite was transformed into ε-martensite rather than α′-martensite during the postsolidification phase transformations of ingots with a Mn content of > 20%. The phase composition of Fe-20Mn and Fe-25Mn specimens was entirely the ε phase, whereas Fe-30Mn and Fe-35Mn specimens comprised γ + ε phases, with the single γ phase being tangentially increased.

XRD results similar to those found here have been reported previously, but no correlation was made with MRI findings in those studies (10-12). The Mn content of Fe-Mn alloys not only affects the phase distribution, but also the magnetic susceptibility on MRI. The size of the low-intensity area on various MRI sequences decreased with increasing Mn content, concurring with the phase constitution on XRD. The low-intensity area was largest for Fe-10Mn, with mostly α′-martensite in the constituent phase, and smallest for Fe-35Mn, with γ-austenite and/or ε - martensite, although there was a plateau for Mn contents between 25-35%. The findings of this study suggest that suppression of α′-martensite is important for reducing the magnetic susceptibility of the alloy. Mn is thought to be an austenite (γ) stabilizer, since Fe-Mn alloys with a full γ phase can be produced when the Mn content is > 35%.

When considering stent-compatible materials, the mechanical properties need to be taken into account, along with the magnetic susceptibility. As with magnetic susceptibility, the mechanical properties of alloys varied according to the phase constitution. This study suggested that an Mn content of 25% might be the optimal condition for stent-compatible material, since its magnetic susceptibility decreased steadily when Mn content was > 25%, but the mechanical properties, such as microhardness, was highest for Fe-25Mn. In accordance with the findings of previous studies, Fe-35Mn alloys comprising a single γ phase were softer than alloys with a lower Mn content (10).

Interestingly, the susceptibility artifact of stents occurs in a diametric direction rather than a longitudinal direction. The low-intensity diameter ratio was greater than the low-intensity length ratio in the case of a cylindrical specimen located parallel to B0. The values were similar but more severe in the case of a location perpendicular to B0. These findings suggest that for cylindrical devices such as stents, the susceptibility artifact is more likely to be related to the diameter of the low-intensity area rather than to its length, although further studies are necessary to confirm this.

The present study also revealed that homogenization heat treatment did not uniformly control magnetic susceptibility according to the Mn content. At Mn contents lower than 20%, the size of the low-intensity area was decreased by heat treatment on the various types of MRI sequences. However, heat treatment did not change the size of the low-intensity area for Mn contents of > 25%. Hence, homogenizing heat treatment may be useful to enhance the mechanical properties of Fe-Mn alloys but not to reduce their susceptibility artifact, while varying the Mn content may be useful for reducing the size of the low-intensity area on MRI.

We acknowledge several limitations in the methodology of this work which should be considered when interpreting the results reported herein. First, there was a slight difference between nominal and actual Mn contents in the binary Fe-Mn alloy ingots made using the arc-melting technique. However, this difference was within a negligible range, and seems to be attributable to the evaporation of some Mn due to its high vapor pressure during the arc-melting process. Second, it was not possible to acquire the 3D SPGR sequences for alloys with a Mn content of < 15% due to the presence of a severe magnetic susceptibility artifact, which overwhelmed the background high intensity of the $CuSO_4$ solution. In that situation, different types of MRI sequences might be considered in order to reduce the magnetic susceptibility and obtain images by controlling the image parameters. In this study, additional T1WI or T2WI proved that the specimen existed within container. The sizes of the low-intensity area on 3D SPGR were compared between GRE (3D SPGR and T2*-GRE) and FSE (T1WI and T2WI) sequences. Both the length ratio and diameter ratio were lowest for FSE sequences (T1WI and T2WI) and highest for T2*-GRE (1.83 times the average for FSE). Third, the magnetic susceptibility on MRI was quantified by measuring two-dimensional maximum diameters or lengths instead of the volume of the low-intensity area, as performed by several previous authors (18, 19). Fourth, Mn is a heavy metal that may cause neurotoxicity in people who are chronically exposed to it (25-27). Neurobehavioral dysfunction due to Mn exposure predominantly affects the fine motor functions and can cause reduced cognitive performance. The results of an *in vitro* study suggested that Mn(III) ions have a higher oxidative reactivity than Mn(II) ions, and can mimic Fe ions (28). However, once Fe is alloyed with Mn, these elements form a solid solution in which the two atom types are homogeneously arranged in a cubic crystal structure that is different from those of the constituent elements (29). It is expected that Fe-Mn alloys will exhibit different cytotoxic behavior than those of the individual elements, possibly due to a slower release of the Mn ion. Although the results of the MTT assay in this study suggest that Fe-Mn alloys did not affect the cell survival of fibroblasts *in vitro*, the biosafety of Fe-Mn alloys needs to be investigated further in an animal model.

In conclusion, based on these findings, Fe-Mn alloys appear to have potential as a stent material from the perspectives of magnetic susceptibility, mechanical properties, and biological compatibility. Increasing the Mn content in the Fe-Mn alloy from 10% to 35% reduced the size of the susceptibility artifact on MRI. This reduced susceptibility artifact was strongly correlated with the altered microstructure observed by XRD and the composition of the constituent phases, which changed from α'-martensite to γ-austenite and/or ε-martensite. Proper conditioning of the Mn content in Fe-Mn alloys will improve its visibility on MRA; it is recommended that the alloy should have a Mn content of > 25% in order to reduce magnetic susceptibility.

Acknowledgments

This work was supported by the Basic Science Research Program through the National Research Foundation of Korea (NRF) funded by the Ministry of Education, Science, and Technology (grant number 2014R1A1A2057298). The authors have no conflicts of interest to disclose.

REFERENCES

1. Sigwart U, Puel J, Mirkovitch V, Joffre F, Kappenberger L. Intravascular stents to prevent occlusion and restenosis after transluminal angioplasty. N Engl J Med 1987;316:701-706
2. Schomig A, Kastrati A, Mudra H, et al. Four-year experience with Palmaz-Schatz stenting in coronary angioplasty complicated by dissection with threatened or present vessel closure. Circulation 1994;90:2716-2724
3. Hoffmann R, Mintz GS, Dussaillant GR, et al. Patterns and mechanisms of in-stent restenosis. A serial intravascular ultrasound study. Circulation 1996;94:1247-1254
4. Heublein B, Rohde R, Kaese V, Niemeyer M, Hartung W, Haverich A. Biocorrosion of magnesium alloys: a new principle in cardiovascular implant technology? Heart 2003;89:651-656
5. Waksman R, Pakala R, Kuchulakanti PK, et al. Safety and efficacy of bioabsorbable magnesium alloy stents in porcine coronary arteries. Catheter Cardiovasc Interv 2006;68:607-617; discussion 618-619
6. Waksman R. Update on bioabsorbable stents: from bench to clinical. J Interv Cardiol 2006;19:414-421
7. Erne P, Schier M, Resink TJ. The road to bioabsorbable stents: reaching clinical reality? Cardiovasc Intervent Radiol 2006;29:11-16
8. Peuster M, Wohlsein P, Brugmann M, et al. A novel approach to temporary stenting: degradable cardiovascular stents produced from corrodible metal-results 6-18 months after implantation into New Zealand white rabbits. Heart 2001;86:563-569
9. Peuster M, Hesse C, Schloo T, Fink C, Beerbaum P, von

Schnakenburg C. Long-term biocompatibility of a corrodible peripheral iron stent in the porcine descending aorta. Biomaterials 2006;27:4955-4962
10. Hermawan H, Dube D, Mantovani D. Degradable metallic biomaterials: design and development of Fe-Mn alloys for stents. J Biomed Mater Res A 2010;93:1-11
11. Schinhammer M, Hanzi AC, Loffler JF, Uggowitzer PJ. Design strategy for biodegradable Fe-based alloys for medical applications. Acta Biomater 2010;6:1705-1713
12. Liu B, Zheng YF. Effects of alloying elements (Mn, Co, Al, W, Sn, B, C and S) on biodegradability and in vitro biocompatibility of pure iron. Acta Biomater 2011;7:1407-1420
13. Buecker A, Spuentrup E, Ruebben A, Gunther RW. Artifact-free in-stent lumen visualization by standard magnetic resonance angiography using a new metallic magnetic resonance imaging stent. Circulation 2002;105:1772-1775
14. Trost DW, Zhang HL, Prince MR, et al. Three-dimensional MR angiography in imaging platinum alloy stents. J Magn Reson Imaging 2004;20:975-980
15. O'Brien BJ, Stinson JS, Boismier DA, Carroll WM. Characterization of an NbTaWZr alloy designed for magnetic resonance angiography compatible stents. Biomaterials 2008;29:4540-4545
16. O'Brien B, Stinson J, Carroll W. Development of a new niobium-based alloy for vascular stent applications. J Mech Behav Biomed Mater 2008;1:303-312
17. American Society for Testing and Materials (ASTM) standard F2119-07 (2013): Standard test method for evaluation of MR image artifacts from passive implants. http://www.astm.org/Standards/F2119.htm. Accessed June 19, 2015
18. Port JD, Pomper MG. Quantification and minimization of magnetic susceptibility artifacts on GRE images. J Comput Assist Tomogr 2000;24:958-964
19. Wang Y, Truong TN, Yen C, et al. Quantitative evaluation of susceptibility and shielding effects of nitinol, platinum, cobalt-alloy, and stainless steel stents. Magn Reson Med 2003;49:972-976
20. Coecke S, Balls M, Bowe G, et al. Guidance on good cell culture practice. a report of the second ECVAM task force on good cell culture practice. Altern Lab Anim 2005;33:261-287
21. Gu X, Zheng Y, Cheng Y, Zhong S, Xi T. In vitro corrosion and biocompatibility of binary magnesium alloys. Biomaterials 2009;30:484-498
22. Choi JW, Roh HG, Moon WJ, et al. Time-resolved 3D contrast-enhanced MRA on 3.0T: a non-invasive follow-up technique after stent-assisted coil embolization of the intracranial aneurysm. Korean J Radiol 2011;12:662-670
23. Takayama K, Taoka T, Nakagawa H, et al. Usefulness of contrast-enhanced magnetic resonance angiography for follow-up of coil embolization with the enterprise stent for cerebral aneurysms. J Comput Assist Tomogr 2011;35:568-572
24. Seok JH, Choi HS, Jung SL, et al. Artificial luminal narrowing on contrast-enhanced magnetic resonance angiograms on an occasion of stent-assisted coiling of intracranial aneurysm: in vitro comparison using two different stents with variable imaging parameters. Korean J Radiol 2012;13:550-556
25. Crossgrove J, Zheng W. Manganese toxicity upon overexposure. NMR Biomed 2004;17:544-553
26. Reaney SH, Bench G, Smith DR. Brain accumulation and toxicity of Mn(II) and Mn(III) exposures. Toxicol Sci 2006;93:114-124
27. Chang Y, Jin SU, Kim Y, et al. Decreased brain volumes in manganese-exposed welders. Neurotoxicology 2013;37:182-189
28. Chen JY, Tsao GC, Zhao Q, Zheng W. Differential cytotoxicity of Mn(II) and Mn(III): special reference to mitochondrial [Fe-S] containing enzymes. Toxicol Appl Pharmacol 2001;175:160-168
29. Hermawan H, Purnama A, Dube D, Couet J, Mantovani D. Fe-Mn alloys for metallic biodegradable stents: degradation and cell viability studies. Acta Biomater 2010;6:1852-1860